



Validation of a fully nonlinear and dispersive wave model with laboratory non-breaking experiments

Cécile Raoult, Michel Benoit, Marissa L. Yates

► To cite this version:

Cécile Raoult, Michel Benoit, Marissa L. Yates. Validation of a fully nonlinear and dispersive wave model with laboratory non-breaking experiments. Coastal Engineering, 2016, 114, pp.194 - 207. 10.1016/j.coastaleng.2016.04.003 . hal-01784660

HAL Id: hal-01784660

<https://enpc.hal.science/hal-01784660>

Submitted on 3 May 2018

HAL is a multi-disciplinary open access archive for the deposit and dissemination of scientific research documents, whether they are published or not. The documents may come from teaching and research institutions in France or abroad, or from public or private research centers.

L'archive ouverte pluridisciplinaire **HAL**, est destinée au dépôt et à la diffusion de documents scientifiques de niveau recherche, publiés ou non, émanant des établissements d'enseignement et de recherche français ou étrangers, des laboratoires publics ou privés.

Validation of a fully nonlinear and dispersive wave model with laboratory non-breaking experiments

Cécile Raoult^{a,b}, Michel Benoit^{a,b,c}, Marissa L. Yates^{a,d}

^a*Université Paris-Est, Saint-Venant Hydraulics Laboratory (ENPC, EDF R&D, Cerema), 6 quai Watier, BP 49, 78401 Chatou, France*

^b*EDF R&D, Laboratoire National d'Hydraulique et Environnement, 6 quai Watier, BP 49, 78401 Chatou, France*

^c*Institut de Recherche sur les Phénomènes Hors Equilibre (IRPHE), UMR 7342 (CNRS, Aix-Marseille Université, Ecole Centrale Marseille), 49 rue Frédéric Joliot-Curie, BP 146, 13384 Marseille Cedex 13, France*

^d*Cerema, Tech. Dept. Water, Sea and Rivers, 134 rue de Beauvais, CS 60039, 60280 Margny-les-Compiègne, France*

Abstract

With the objective of modeling coastal wave dynamics taking into account nonlinear and dispersive effects, a highly accurate nonlinear potential flow model was developed. The model is based on the time evolution of two surface quantities: the free surface position and the free surface velocity potential. A spectral approach is used to resolve vertically the velocity potential in the domain, by decomposing the potential using an orthogonal basis of Chebyshev polynomials. [With this approach, a wide range of relative water depths can be simulated, as demonstrated here with the propagation of nonlinear regular waves over a flat bottom with \$kh = 2\pi\$ and \$4\pi\$ \(where \$k\$ is the wave number and \$h\$ the water depth\).](#) The model is [then](#) validated by comparing the simulation results to experimental data for four non-breaking wave test cases: (1) nonlinear dynamics of a wave train generated by a piston-type wavemaker in constant water depth, (2) shoaling of a regular wave train on beach with constant slope up to the breaking point, (3) propagation of regular waves over a submerged bar, and (4) propagation of nonlinear irregular waves over a barred beach. The test cases show the ability of the model to

Email addresses: cecile.raoult@edf.fr (Cécile Raoult), benoit@irphe.univ-mrs.fr (Michel Benoit), marissa.yates-michelin@cerema.fr (Marissa L. Yates)

reproduce well nonlinear wave interactions and the dynamics of higher-order bound and free harmonics. The simulation results agree well with the experimental data, confirming the model's ability to simulate accurately nonlinear and dispersive effects for non-breaking waves.

Keywords: nonlinear, dispersive, water waves, potential theory, Zakharov equations

1. Introduction

Fast and accurate models of wave transformation from deep water to the beach over large spatial scales are needed for coastal and ocean engineering applications, such as the design of shore protection structures or marine renewable energy projects. This objective is not an easy task given the range of spatial and temporal scales [to be modelled](#). [To succeed](#), this type of model requires an accurate representation of nonlinear phenomena playing an important role in wave interactions with structures and bathymetry, an accurate representation of dispersion to propagate waves over a wide range of depths, and the proper simulation of important coastal physical processes like shoaling, refraction, diffraction, breaking, and run-up.

Most fluid flow problems can be described by the Navier-Stokes equations since they account for nonlinearities, vorticity and viscosity. Models based on these equations can be very accurate when studying wave interactions with structures in the surf zone (e.g. Shao (2006); Lara et al. (2006)). These equations can be solved either with an Eulerian approach as in the widely used code OpenFOAM®(Higuera et al., 2013a,b) solving the RANS (Reynolds Averaged Navier-Stokes) equations for two incompressible phases, or with a Lagrangian approach computing the trajectories of interacting fluid particles (e.g. Dalrymple and Rogers (2006)). These models are highly accurate when studying local-scale processes, but the domain size and resolution are limited due to the computational time, even with the use of GPU parallelized codes (Dalrymple et al., 2011). To model large spatial domains, these codes are usually coupled with more computationally efficient models, such as potential flow models, to simulate the far-field processes (Narayanaswamy et al., 2010).

Some assumptions can be made to simplify the problem and thus reduce the computational time. For example, the nonlinear shallow water equations (NLSWE) are derived by depth integrating the Navier-Stokes equations to

model waves with a wavelength significantly longer than the water depth (e.g. to model tidal waves), but this set of equations does not take into account wave dispersion. However, by including non-hydrostatic pressure in the NL-SWE and dividing the water depth into a sufficient number of layers, the frequency dispersion of waves can be greatly improved (Stelling and Zijlema, 2003; Zijlema and Stelling, 2005, 2008; Zijlema et al., 2011). For example, with only two layers, the accuracy of the deep water dispersion relation is similar to that of extended Boussinesq-type models. The dispersion of such non-hydrostatic models can be further improved by optimizing the location of the levels (Zhu et al., 2014).

When viscous and turbulent effects are negligible, the flow can be well represented by potential flow theory, which consists of solving the Laplace problem in the fluid domain, supplemented by nonlinear free surface boundary conditions. One way of solving this problem is to use the Boundary Integral Equations Method (BIEM), which projects the problem on the boundary surface of the fluid domain using Green's Function (Grilli et al., 1989; Wang et al., 1995). These models enable an accurate description of nonlinear and even overturning waves and are well adapted to simulate wave-structure interactions (e.g. Dombre et al. (2015)). This method is mainly used for calculating local-scale interactions owing to the long computational times. However, with the use Fast Fourier Transform (FFT) (Newman and Lee, 2002; Fructus and Grue, 2007) or Fast Multipole Algorithm methods (Fochesato et al., 2007), the computational time can be reduced considerably.

Another way of solving the problem is to make additional assumptions about the nonlinear and dispersive properties of waves. By doing a Taylor expansion of the vertical velocity about a specified level and truncating it to a finite number of terms, Boussinesq-type models assume a polynomial variation of the vertical velocity, thus reducing the problem by one dimension. Boussinesq-type models are derived with the assumption that nonlinearity and/or frequency dispersion are weak or moderate (Madsen and Schäffer, 1998; Kirby, 2003). Using only a quadratic polynomial approximation of the vertical flow distribution gives poor results for wave propagation in intermediate depths. A lot of work has been done to improve the frequency dispersion following various approaches such as: using higher degree polynomials for the vertical approximation with the Green-Naghdi equations (Zhao et al., 2014), using Padé approximants (Agnon et al., 1999) combined with an expansion of the Laplace solution from an arbitrary level (Madsen et al., 2002), and resolving in two arbitrary layers to maintain low-order spatial

derivatives (Lynett and Liu, 2004; Chazel et al., 2009). Additional modeling approaches include those of Kennedy et al. (2001), Fuhrman and Bingham (2004), and Engsig-Karup et al. (2006).

In the present work, a fully nonlinear potential flow theory model is developed solving the Zakharov equations (Zakharov, 1968). The temporal evolution of the free surface elevation η and the free surface velocity potential $\tilde{\Phi}$ are given as a function of these two variables and the vertical velocity at the free surface \tilde{w} . The primary challenge is to express the vertical velocity \tilde{w} as a function of η and $\tilde{\Phi}$, a problem commonly called ‘Dirichlet-to-Neumann’ or DtN. One possibility is to solve directly the Laplace equation using finite element (Wu et al., 1998; Ma et al., 2001) or finite difference (Li and Fleming, 1997; Engsig-Karup et al., 2009) methods. When using finite difference methods, Kreiss and Oliger (1972) and Bingham and Zhang (2007) recommend using fourth-order schemes with a stretched vertical grid (clustering points near the free surface) instead of using second-order schemes with a regular grid. When considering rectangular domains with a flat bottom, a high-order spectral approach (HOS) is optimal (Dommermuth and Yue, 1987; West et al., 1987; Chern et al., 1999; Ducroz et al., 2012). This method is faster than finite difference methods but less flexible with regard to the specified geometry and bathymetry, even if progress has been made in taking into account variable and moving bottoms (Smith, 1998; Guyenne and Nicholls, 2007; Gouin et al., 2015). An additional approach is to use a spectral method only in the vertical dimension either by expanding the velocity potential with a local mode series (Belibassakis and Athanassoulis, 2011) or by projecting it on a polynomial basis (Kennedy and Fenton, 1997; Tian and Sato, 2008). By using high-order finite difference schemes in the horizontal, these models maintain a flexible approach for variable domain geometries and bathymetry. A comparison between a vertical spectral approach and a finite difference approach in the vertical dimension shows the improved accuracy and efficiency of the spectral method in 1DH (Yates and Benoit, 2015) and 2DH (Christiansen et al., 2013). Others approaches can be used, such as the extension of the DtN operator as a sum of global convolution terms and local integrals with kernels decaying quickly in space (Clamond and Grue, 2001; Fructus et al., 2005). Here, the combination of high-order finite difference schemes for the horizontal dimension and a spectral approach using Chebyshev polynomials in the vertical dimension is tested with emphasis on the ability of the model to accurately represent nonlinear and dispersive phenomena.

The mathematical model and its numerical implementation are presented

in Section 2. In Section 3, the ability of the model to simulate deep water cases is demonstrated before the model is validated by comparing simulation results to experimental data for four non-breaking wave test cases: (1) nonlinear dynamics of free and bound components in a wave train generated by a piston-type wavemaker in constant water depth, (2) shoaling of a regular wave train on beach with constant slope up to the breaking point, (3) propagation of regular waves over a submerged bar (Dingemans, 1994), and (4) propagation of nonlinear irregular waves over a barred beach (Becq-Girard et al., 1999). Conclusions and ongoing developments are summarized in the final Section.

2. Mathematical model and numerical implementation

2.1. Mathematical model

By assuming an inviscid and homogeneous fluid of constant density, and irrotational flow, potential flow theory can be used. The velocity potential $\Phi(\underline{x}, z, t)$, where $\underline{x} = (x, y)$, must satisfy the Laplace equation in the fluid domain:

$$\nabla^2 \Phi + \Phi_{zz} = 0. \quad (1)$$

Here, $\nabla f \equiv (f_x, f_y)$ is the horizontal gradient operator, and partial derivatives are denoted with subscripts. At the free surface $z = \eta(\underline{x}, t)$, which is assumed to be single-valued in \underline{x} (no overturning waves), and the (nonlinear) kinematic and dynamic boundary conditions (BC) for $z = \eta(\underline{x}, t)$ are:

$$\eta_t = -\nabla \eta \cdot \nabla \Phi + \Phi_z, \quad (2)$$

$$\Phi_t = -g\eta - \frac{1}{2} ((\nabla \Phi)^2 + (\Phi_z)^2). \quad (3)$$

In (3), the atmospheric pressure at the free surface is assumed to be uniform (and chosen to be 0 by convention), surface tension is neglected, and g is the acceleration of gravity. At the bottom $z = -h(\underline{x})$, assumed constant in time, the kinematic (impermeability) BC is:

$$\nabla \Phi \cdot \nabla h + \Phi_z = 0. \quad (4)$$

At the lateral boundaries, periodic, Dirichlet or Neumann BCs can be imposed.

By defining the velocity potential at the free surface $\tilde{\Phi}(\underline{x}, t) \equiv \Phi(\underline{x}, z = \eta(\underline{x}, t), t)$, the free surface conditions (2) and (3) are reformulated respectively as (Zakharov, 1968):

$$\eta_t = -\nabla \eta \cdot \nabla \tilde{\Phi} + \tilde{w} (1 + (\nabla \eta)^2), \quad (5)$$

$$\tilde{\Phi}_t = -g\eta - \frac{1}{2}(\nabla \tilde{\Phi})^2 + \frac{1}{2}\tilde{w}^2 (1 + (\nabla \eta)^2), \quad (6)$$

where $\tilde{w}(\underline{x}, t) \equiv \Phi_z|_{z=\eta(\underline{x}, t)}$ is the vertical velocity at the free surface.

Equations (5-6) involve only free surface quantities, which are functions of \underline{x} and t only. To integrate these equations in time, it is necessary to determine $\tilde{w}(\underline{x}, t)$ from $(\eta(\underline{x}, t), \tilde{\Phi}(\underline{x}, t))$, the DtN problem.

As described in Yates and Benoit (2015), the DtN problem is resolved by solving a Laplace boundary value problem (BVP) for the potential Φ , namely the Laplace equation (1), supplemented with the Dirichlet BC at the free surface:

$$\Phi = \tilde{\Phi} \quad \text{at } z = \eta(\underline{x}, t), \quad (7)$$

the bottom BC (4), and specified lateral BCs. Following the work of Tian and Sato (2008) a spectral method is applied in the vertical dimension. An outline of the method, detailed in Yates and Benoit (2015), is given hereafter for the case of a single horizontal dimension (i.e. $\underline{x} = x$), and the extension to two horizontal dimensions is straightforward.

First, the fluid domain is mapped onto a strip of constant height by introducing the vertical coordinate s , which varies from $s = -1$ at the bottom to $s = 1$ at the free surface:

$$s(x, z, t) = \frac{2z + h^-(x, t)}{h^+(x, t)}, \quad (8)$$

where $h^+(x, t) = h(x) + \eta(x, t)$ and $h^-(x, t) = h(x) - \eta(x, t)$. The BVP is then reformulated in this transformed space (x, s) for $\Phi(x, z, t) \equiv \varphi(x, s(x, z, t), t)$. The Laplace equation (1) in the fluid domain, the bottom BC (4) and the free surface Dirichlet BC (7) become:

$$\varphi_{xx} + 2s_x \varphi_{xs} + (s_x^2 + s_z^2) \varphi_{ss} + s_{xx} \varphi_s = 0 \quad \text{in the fluid domain,} \quad (9)$$

$$h^+ h_x \varphi_x + 2(1 + h_x^2) \varphi_s = 0 \quad \text{for } s = -1, \quad (10)$$

$$\varphi(x, 1) = \tilde{\Phi}(x) \quad \text{for } s = 1. \quad (11)$$

Then a spectral approach is used in the vertical: the vertical variation of the velocity potential is approximated by a linear combination of Chebyshev

polynomials of the first kind, $T_n(x)$, where $n = 0, 1, 2, \dots$ indicates the order of the polynomial:

$$\varphi(x, s) \approx \sum_{n=0}^{N_T} a_n(x) T_n(s), \quad (12)$$

where N_T is the maximum order of the Chebyshev polynomials. These polynomials are easy to evaluate, converge rapidly, and have a large convergence domain. Tian and Sato (2008) and Yates and Benoit (2015) have shown that values of N_T lower than 10 (typically in the range $[5, 8]$) are sufficient to provide high accuracy for a variety of test cases. Furthermore, with the inner product defined as:

$$\langle f, g \rangle \equiv \int_{-1}^1 \frac{f(s)g(s)}{\sqrt{1-s^2}} ds, \quad (13)$$

the T_n polynomials form an orthogonal basis over the range $[-1, 1]$, since it can be shown that:

$$\langle T_n, T_p \rangle = \begin{cases} 0 & \text{if } n \neq p, \\ \pi & \text{if } n = p = 0, \\ \frac{\pi}{2} & \text{if } n = p \neq 0. \end{cases} \quad (14)$$

For an arbitrary function $f(s)$ in $[-1, 1]$, the following operator is defined:

$$\langle f \rangle_p \equiv \frac{2}{\pi C_p} \langle f, T_p \rangle, \quad \text{with } \begin{cases} C_0 = 2, \\ C_p = 1 & \text{for } p > 0. \end{cases} \quad (15)$$

The orthogonality relations (14) then become: $\langle T_n \rangle_p = \delta_{np}$, where δ_{np} is the Kronecker delta.

By substituting the approximation (12) in the BVP (9-11), the Laplace equation (9) becomes (dropping the x argument of $a_n(x)$ coefficients and the s argument of $T_n(s)$ polynomials for brevity):

$$\sum_{n=0}^{N_T} [a_n'' T_n + 2s_x a_n' T_n' + a_n((s_x^2 + s_z^2) T_n'' + s_{xx} T_n')] = 0, \quad (16)$$

with:

$$s_x = (h_x^- - s h_x^+)/h^+, \quad s_z = 2/h^+, \quad s_{zz} = 0, \quad (17)$$

$$s_{xx} = [(h_{xx}^- h^+ - 2h_x^- h_x^+) + s(2(h_x^+)^2 - h_{xx}^+ h^+)]/(h^+)^2, \quad (18)$$

and

$$a'_n \equiv \frac{da_n}{dx}, \quad a''_n \equiv \frac{d^2a_n}{dx^2}, \quad T'_n \equiv \frac{dT_n}{ds} \quad \text{and} \quad T''_n \equiv \frac{d^2T_n}{ds^2}. \quad (19)$$

Then the Chebyshev-tau method, a variant of the Galerkin method (see e.g. Boyd (2001)), is applied in the vertical to (16) to remove the s dependence. The operator $\langle \cdot \rangle_p$ is applied to (16) for $p = 0, 1, \dots, N_T - 2$, yielding $N_T - 1$ equations:

$$a''_p + \sum_{n=0}^{N_T} C_{pn} a'_n + \sum_{n=0}^{N_T} D_{pn} a_n = 0, \quad p = 0, 1, \dots, N_T - 2, \quad (20)$$

with $C_{pn} \equiv (m_{011}B_{p01n} + m_{111}B_{p11n})/m_{020}$ and $D_{pn} \equiv (m_{002}B_{p02n} + m_{102}B_{p12n} + m_{202}B_{p22n} + m_{001}B_{p01n} + m_{101}B_{p11n})/m_{020}$. The terms m_{ijk} depend only on $h^+(x, t)$, $h^-(x, t)$, their spatial derivatives (see equations (21)-(28) in Tian and Sato (2008)), and the coefficients:

$$B_{pikn} \equiv \langle s^i \frac{\partial^k T_n}{\partial s^k}(s) \rangle_p, \quad (21)$$

which are constant and can be calculated analytically once at the beginning of each simulation.

The $N_T - 1$ equations (20) are supplemented by the two BCs at the bottom (10) and the free surface (11), which become respectively:

$$\sum_{n=0}^{N_T} [(-1)^n h^+ h_x a'_n + (-1)^{n-1} 2n^2 (1 + h_x^2) a_n] = 0, \quad (22)$$

$$\sum_{n=0}^{N_T} a_n = \tilde{\Phi}. \quad (23)$$

Thus, at each node x , there are $N_T + 1$ equations to solve for the $N_T + 1$ unknown coefficients $a_n(x)$ for $n = 0, 1, \dots, N_T$. A similar treatment is applied for lateral boundary points (see Yates and Benoit (2015)).

Once the $a_n(x)$ are determined, the vertical velocity at the free surface \tilde{w} is readily obtained:

$$\tilde{w}(x) = \phi_s s_z|_{s=1} = \frac{2}{h^+(x)} \sum_{n=0}^{N_T} a_n(x) n^2, \quad (24)$$

and equations (5-6) can be stepped forward in time.

2.2. Numerical implementation

To simulate this mathematical model, a numerical model, named MISTHYC, has been developed and coded in Fortran in one horizontal dimension (x, z) . The horizontal domain is discretized with N_X nodes in the x direction, with constant or variable Δx . High-order finite difference approximations (fourth order here) are used to calculate first and second-order derivatives in x , following Fornberg (1988). The explicit four-step fourth-order Runge-Kutta (RK4) scheme with a constant time step is used to integrate (5) and (6) in time.

At each step of the RK4 scheme, the discretization of the Laplace BVP in (x, s) , with N_X nodes in x and N_T the maximum order of the Chebyshev polynomials, results in a system of $N_X(N_T + 1)$ linear equations for the coefficients $a_n(x_i)$ for $n = 0, \dots, N_T$ and $i = 1, \dots, N_X$. The corresponding matrix is sparse, and the system is currently solved in MISTHYC using the direct solver MUMPS (“MUltifrontal Massively Parallel Solver”, v4.10.0) (Amestoy et al., 2001, 2006) using the default settings. Iterative solvers could be also used and will be tested in the future.

3. Validation test cases

The model is validated by comparing the simulation results to stream function solutions of regular nonlinear waves propagating in deep water, and then to measurements from four laboratory experiments of non-breaking waves: (1) nonlinear dynamics of free and bound components in a wave train generated by a piston-type wavemaker in constant water depth, (2) shoaling of a regular wave train on beach with constant slope up to the breaking point, (3) propagation of regular waves over a submerged bar (Dingemans, 1994), and (4) propagation of nonlinear irregular waves over a barred beach (Becq-Girard et al., 1999).

3.1. Applicability of the model to large relative water depths

Incident wave conditions are characterized by two non-dimensional numbers: (i) the relative water depth $\mu \equiv kh$ (equivalently h/L) and (ii) the wave steepness $\epsilon \equiv ka = kH/2$ (equivalently H/L), where h is the local water depth, k is the wave number of the fundamental wave for regular waves (or the peak frequency for irregular waves), $L = 2\pi/k$ is the wavelength, H is the wave height (crest-to-trough height for regular waves or significant wave

height H_{m0} for irregular waves), and $a = H/2$ is the wave amplitude. Given h and T , k and L are computed from the linear dispersion relation.

In the following four laboratory experiments, the relative water depth kh is moderate or small (in the range $[0.53, 0.73]$) where incident waves are imposed. As waves propagate, higher harmonics are generated with frequencies that are multiples of the fundamental frequency, with consequently larger values of kh . To represent properly the dynamics of the higher harmonics, the model must simulate accurately wave dispersion for values of kh much larger than that of the fundamental frequency.

Yates and Benoit (2015) showed that deep water $\mu > \pi$ (or $h/L > 1/2$) test cases can be modeled accurately by increasing the maximum order N_T of the Chebyshev polynomials (12) for: (1) the propagation of a stable, regular nonlinear wave in constant depth, and (2) the periodic motion of a nonlinear standing wave in constant depth. In the first case, the initial wave profile, obtained from the stream function method (order 20), corresponds to a relative water depth $\mu = 2\pi \approx 6.28$ (or $h/L = 1$) and steepness $\epsilon = \pi/10 \approx 0.314$ (or $H/L = 10\%$). After propagating for 25 wave periods, errors in the free surface position remained small ($< 0.1\%$) for $N_T > 7$ (see e.g. section 3.1.3 and Figures 7 and 8 in Yates and Benoit (2015)). In the second case, after 100 periods of motion of a standing wave with $\mu = 3$ (or $h/L \approx 0.5$) and $\epsilon = 0.42$, and with $N_T = 7$ and sufficient horizontal resolution, the free surface position errors also remained relatively small ($< 3\%$). Considering the increase in computational time with N_T , Yates and Benoit (2015) concluded that the optimal range of N_T is $[7; 15]$ in such deep water conditions.

To further demonstrate the ability of the model to simulate accurately waves in deep water, new results are presented here for 25 periods of propagation of a stable, regular nonlinear wave with wave steepness $\epsilon = \pi/10 \approx 0.314$ (or $H/L = 10\%$, same as in Yates and Benoit (2015)) and $\mu = 4\pi \approx 12.56$ (or $h/L = 2$), which is 4 times the deep water threshold (and twice that shown in Yates and Benoit (2015)). The computational domain is one wavelength ($L = 64$ m), and based on the sensitivity tests shown in Yates and Benoit (2015), the spatial and temporal discretization are $\Delta x = L/96$ and $\Delta t = T/75$, respectively, corresponding to $CFL = 1.28$. The initial wave is computed from the stream function solution (order 20), and after each period the computed wave should be unchanged from the initial wave profile. Final wave profiles for $N_T = 5, 7, 8, 10, 12, 15$, and 20 are presented in Figure 1a and b for $\mu = 2\pi$ and 4π , respectively. Both cases converge visually when N_T is increased, but for the deeper water case, the errors decrease more slowly

and the simulation with $N_T = 5$ does not remain stable for long time simulations. A quantitative comparison of the phase difference with respect to its theoretical position after 25 periods of wave propagation (Figure 2) shows that the accuracy of the simulations generally increases to an approximately constant value with increasing N_T . For $N_T < 12$, the phase errors are larger for the deeper water case ($kh = 4\pi$), but for $N_T \geq 12$, the phase differences decrease and the model simulates accurately long term wave propagation for both cases. These tests show that the model is able to simulate accurately deep water waves by increasing the order of the maximum Chebyshev polynomial (e.g. using $N_T = 10$ for $kh = 2\pi$ and $N_T = 12$ for $kh = 4\pi$).

3.2. Nonlinear dynamics of a wave train generated by a piston-type wavemaker in constant water depth

The first case consists of simulating the propagation of waves generated by the sinusoidal movement of a piston-type wavemaker over a flat bottom, based on the flume experiments of Chapalain et al. (1992) (C92). The results presented here correspond to trial A (piston stroke amplitude $e = 7.8$ cm and period $T = 2.5$ s), with a constant water depth $h = 0.4$ m. The wavelength of the fundamental component is $L = 4.74$ m from the linear dispersion relation, corresponding to long waves with $\mu = 0.53$. The model domain is regularly meshed with $\Delta x = 0.1$ m ($\approx L/47$) and extends far enough to prevent reflection from the right boundary. The waves were propagated during 16 periods (i.e. 40 s) with a time step $\Delta t = T/40 = 0.0625$ s, with maximum order of the Chebyshev polynomial $N_T = 7$. The model is forced by imposing at the left boundary a sinusoidal time varying horizontal velocity that is uniform in the vertical.

A harmonic analysis of free surface elevation time series (after the steady state is reached) decomposes the signal into a discrete sum:

$$\eta(t) = a_0 + \sum_{n=1}^N a_n \cos(n\omega t + \varphi_n), \quad (25)$$

where t is time, $\omega = \frac{2\pi}{T}$ is the angular frequency of the wavemaker, and a_n and φ_n are the amplitude and phase of the harmonic component n . The phase difference between the first and the second harmonic is defined as $\Delta \varphi_{1,2} \equiv \varphi_2 - 2\varphi_1$, following Chapalain et al. (1992). The simulated spatial evolution of the amplitudes of the first four harmonics agrees well with the experiments (Figure 3a). Overall, the model correctly represents the energy

transfers between the different harmonic components, as well as the resultant beat lengths. However, a decrease in the second harmonic amplitude (after $x = 19$ m) is observed in the experimental data but is not reproduced in the simulations. This could be explained by dissipation in the experiments that is not taken into account in the model. This phenomenon is more noticeable for short waves, hence more visible for the higher harmonics. The spatial evolution of the phase difference between the first and second harmonic is also reproduced well. The phase difference oscillates between $-\pi/2$ and $+\pi/2$ with the same periodicity as the harmonic amplitudes. Zero phase difference occurs when either the first harmonic is maximum and the second harmonic is minimum, or the contrary.

The variation of the free surface elevation thus depends on the location in the wave channel, as shown in Figure 4 at $x = 4$ m, 7 m, 10 m and 14 m. The simulated free surface position qualitatively agrees well with the measurements (compared to Figure 3 of Chapalain et al. (1992)). When the first and second harmonics are in phase, the free surface profile is either quasi-sinusoidal when the first harmonic is maximal and the second minimal (e.g. $x = 14$ m), or cnoidal when the second harmonic is maximal and the first minimal (e.g. $x = 7$ m). However, when the first and second harmonics are out of phase, the waves are vertically asymmetrical with either a steeper (gentler) wave front and a gentler (steeper) rear slope if the phase difference is positive (negative) (e.g. $x = 10$ m and $x = 4$ m).

3.3. Nonlinear wave shoaling on a gently sloping beach

The second test case simulates the shoaling of regular nonlinear waves on a gently sloping (1/35) beach following the experiments of Ting and Kirby (1994) (TK94). In the spilling breakers experiment, waves were generated in $h = 0.4$ m water depth with a wave period of $T = 2.0$ s and wave height of $H = 0.125$ m, corresponding to long waves with $\mu = 0.68$ ($h/L = 0.104$) and $\epsilon = 0.1$ (or $H/L = 3.3$ %). In the numerical model, waves are generated with the same wave characteristics as the experiments by searching for the analytical solution to the Zakharov equations and numerically (iteratively) finding the solution. Dirichlet boundary conditions are applied to generate waves at the left boundary and in a relaxation zone that extends $2 - 3L$ into the domain ($-15.0 \leq x \leq -4.5$ m). In the experiments, waves begin to break around $x = 6.0$ m. The present numerical model is not able to take into account the effects of wave breaking; therefore, waves are absorbed in an absorption zone of constant depth ($h = 0.2286$ m) from $x = 6.0$ m to

$x = 15.0$ m (shaded gray area, Figure 5). The model results will only be compared to the experimental data before the absorption zone. For these nonlinear waves, the model domain was discretized with $\Delta x = 0.03$ m ($\approx L/100$, with $L = 3.8434$ m, the wavelength calculated by the numerical solution for $h = 0.4$ m), the time step was $\Delta t = 0.01$ s ($T/200$), and $N_T = 7$. As the waves become highly nonlinear approaching the breaking limit, high frequency instabilities develop in the numerical model. For the selected spatial and temporal discretization, a fourth-order Savitzky-Golay filter was applied over 9 points (twice the stencil size) at the end of each time step to smooth these high frequency instabilities.

The measured crest and trough elevation envelope is reproduced well by the model during the shoaling phase up to the breaking point ($x = 6.0$ m, Figure 5a). After this point, the absorption zone dissipates wave energy but does not try to reproduce the effects of wave breaking, and the simulated and measured free surface elevation decay at different rates. Simulated free surface elevation time series at four positions in the wave tank (Figure 6) agree well with the wave gauge measurements. At the bottom of the sloping beach profile, waves are nearly symmetric (Figure 6a). As they progress up the slope and shoal, the wave profiles become asymmetric with steeper wave fronts and gentler rear faces, and more skewed with more pointed peaks and wider troughs (Figure 6b-d). Even near the breaking point, the simulated wave profiles agree well with the measurements, with only small differences in the wave troughs (Figure 6c-d).

To quantify the wave nonlinearity, higher order statistical moments were calculated from the free surface elevation time series, including the skewness (or horizontal asymmetry) and kurtosis (or measure of the flatness of the free surface elevation distribution). The skewness is defined as the normalized, centered, third-order moment of the free surface elevation:

$$S = \frac{\langle (\eta - \langle \eta \rangle)^3 \rangle}{\sigma^3}, \quad (26)$$

and the kurtosis as the normalized, centered, fourth-order moment of the free surface elevation:

$$K = \frac{\langle (\eta - \langle \eta \rangle)^4 \rangle}{\sigma^4}, \quad (27)$$

where the variance σ^2 of the free surface elevation is:

$$\sigma^2 = \langle (\eta - \langle \eta \rangle)^2 \rangle, \quad (28)$$

with $\langle - \rangle$ denoting the time-average operator.

As observed in the free surface time series, the waves progressively develop narrow, peaked crests and wide, flat troughs as they shoal on the slope, causing an increase in skewness (Figure 7a). With these changes in the wave profile, the free surface elevation distribution becomes less Gaussian, thus causing an increase in the kurtosis (Figure 7b). The simulations reproduce well the measured increases in skewness and kurtosis as the waves shoal, with small differences appearing as the waves become highly nonlinear approaching the breaking point. After the breaking point, the model is not able to simulate accurately the wave profile and the dissipation of energy, and a wave breaking dissipation model is currently being developed to take into account these effects.

3.4. Regular waves over a submerged bar

Beji and Battjes (1993) and then Dingemans (1994) (D94) performed a series of experiments of regular wave propagation over a submerged trapezoidal bar. These experiments are now a standard test case for wave models since both nonlinear and dispersive effects are important when waves propagate over the top of the bar. The bottom profile is shown in Figure 8 at the scale of the experiments of Beji and Battjes (1993). The water depth is $h = 0.40$ m offshore and reduces to a minimum of 0.10 m on top of the bar. The front slope of the bar is 1:20, and the rear slope is 1:10. Eleven wave probes recorded the free surface elevation time series in the experiments (see positions in Figure 8).

Here, case A is studied with an incident wave height $H = 2.0$ cm and a period $T = 2.02$ s, corresponding to long waves with $\mu = 0.67$ (or $h/L = 0.107$) offshore of the bar and relatively small steepness $\epsilon = 0.017$ (or $H/L = 0.53\%$). Under these conditions, the incident wave train is significantly affected during the propagation over the submerged bar, with transfers of energy toward higher harmonics.

The model domain has a regularly spaced grid with $\Delta x = 0.05$ m (i.e. about $L/75$ offshore of the bar) and extends from $x = -6$ m to 30 m (721 nodes along the x axis). Waves are generated in an 8-m wide relaxation zone at the left boundary of the domain ($-6 \leq x \leq 2$ m) using a second-order Stokes solution to impose the free surface elevation and the velocity potential. Waves are absorbed in a 5-m wide relaxation zone ($25 \leq x \leq 30$ m) applied in front of the fully reflective right boundary to avoid reflections.

Waves are propagated during 25 wave periods (i.e. 50.5 s) with a time step $\Delta t = T/100 = 0.0202$ s.

Times series of free surface profiles computed with $N_T = 7$ are presented at probes 4 to 11 in Figure 9. The choice of this value of N_T will be discussed at the end of this section. When waves propagate over the front slope of the bar, the wave height and steepness increase due to shoaling effects (probes 4 to 6, Figure 9(a-c)). The wave profile becomes asymmetric due to nonlinear wave-bottom interactions that create higher frequency bound harmonic components. These harmonics are released in the shallowest region and on the rear slope of the bar and then propagate at their own phase speed (probes 7 and 8, Figure 9(d-e)). After the bar, the measured wave profiles vary significantly between the probes due to the differences in celerity of the free wave components. At the last three probes (probes 9 to 11, Figure 9(f-h)), the model reproduces well the complex wave profiles, including the dispersive (high frequency) components.

In order to examine more closely the energy transfers between harmonics, a Fourier analysis of the measured and computed wave signals was completed. The model accurately reproduces the spatial evolution of the amplitudes of the first six harmonics, corresponding to frequencies $f = 1/T$ (fundamental component) to $6f$ (Figure 10). The amplitude of the fundamental harmonic increases due to shoaling on the submerged bar up to the bar's crest and then decreases (starting from about $x = 12$ m) due to transfers of energy toward higher harmonics. The observed oscillations are hypothesized to be caused by reflections in the wave channel. The second harmonic ($2f$) increases as the waves shoal on the front slope of the bar and continues increasing until $x = 16$ m, after which its amplitude fluctuates. The higher harmonics start increasing in amplitude at shallower depths, and mainly develop around the bar crest ($12 \leq x \leq 15$ m). Harmonics $4f$ to $6f$ decrease after the bar, which is not the case for harmonics $2f$ and $3f$. In addition, after the bar, the second harmonic has the largest amplitude, and the amplitude of the third harmonic is nearly comparable to (though smaller than) that of the fundamental component. The model results agree well with the data up to the sixth harmonic, with the exception of slight differences at some locations in the amplitude of the second harmonic (e.g. at $x = 19$ m).

To test the sensitivity of the model to the parameter N_T (all other parameters were kept constant), simulations were run with $N_T = 3, 4, 5, 7$ and 10 and compared to the observations (Figure 11). In the offshore part of the flume and up to the submerged bar (i.e. up to probe 8), only the simulation

results with $N_T = 3$ differ significantly from those with higher N_T , which are superimposed and agree well with the measured time series. At the last three probes, where dispersive effects are more important, the results with $N_T = 3$ clearly deteriorate, and results with $N_T = 4$ and 5 also show increasing differences with the measurements. Results with $N_T = 7$ and 10 remain superimposed and in good agreement with the measurements at all probes. Therefore, $N_T = 7$ was chosen to optimize model's accuracy and efficiency.

3.5. Random waves over a barred beach

The last test case simulates the propagation of irregular nonlinear waves over a barred beach, reproducing the wave flume experiments of Becq-Girard et al. (1999) (B99). The bathymetric profile of these experiments (Figure 12) was specifically designed to study nonlinear wave effects in shallow water (triad interactions). Irregular waves were generated with a piston-type random wavemaker using a JONSWAP wave spectrum with a peak-enhancement factor of $\gamma = 3.3$. The bottom profile was created with smooth metal sheets to minimize bottom friction dissipation, and a beach absorber was included on the upper part of the beach to reduce wave reflection. Resistive-type wave probes measured the free surface elevation at 16 locations in the wave flume (Figure 12) during the 40-minute experiment with a sampling time step $\Delta t = 0.07$ s.

The model computational grid extends from $x = -5$ m to $x = 25$ m (with the foot of the bar at $x = 0$ m). Waves are generated in a 5-m relaxation zone by imposing the velocity potential at the left boundary and correcting the free surface position and velocity potential in the relaxation zone. Non-breaking irregular waves are simulated with significant wave height of $H_{m0} = 3.4$ cm and a peak period of $T_p = 2.39$ s in the deepest part of the domain ($h = 0.65$ m). Waves are absorbed in a 10-m long relaxation zone at the right boundary. Time series of these variables are reconstructed using linear wave theory to sum the components of the wave spectrum obtained from the free surface measurements at probe 2 (located at the foot of the submerged bar). The computational grid is regularly meshed with $\Delta x = 0.05$ m, and $N_T = 7$, as in the previous test case. The total simulation time is 2380 s (approximately 39.7 min), with a time step equaling the sampling time step of the free surface elevation probes, $\Delta t = 0.07$ s.

The measured and simulated wave variance spectra agree well (Figure 13, spectra at probes 2, 5, 7, 9, 11, 13, 15, and 16). The main spectral peak increases from probes 2 to 5 due to wave shoaling. In addition, energy is

transferred from lower to higher frequencies, particularly from the peak frequency to its super-harmonics. This phenomenon is visible at probe 5 with the appearance of the second harmonic peak ($2f_p$). When the water depth becomes nearly constant (probes 7, 9, and 11), the second and higher harmonic peaks become more pronounced. A peak at the fifth harmonic ($5f_p$) becomes visible in the spectra at probes 9 and 11, and its amplitude is reproduced well by the model. On the back side of the bar, the energy transfer reverses back to the lower harmonics (in particular to the second harmonic). At probe 13, the peak of the fifth harmonic disappears, and at probe 15, the peaks of the third and fourth harmonics also nearly disappear. Only the second harmonic and main spectral peaks remain visible in the trough. Finally, at probe 16, the third harmonic ($3f_p$) peak reappears due to the new decrease in the water depth.

The simulated spatial evolution of the first five harmonic amplitudes agrees well with the experimental observations (Figure 14). In the deep end of the wave tank, the amplitude of the first harmonic is dominant. Between 0 m and 5 m, the first harmonic amplitude increases due to shoaling while the higher harmonics remain stable. After 5 m, the first harmonic amplitude decreases while higher harmonic amplitudes increase due to transfers of energy from lower to higher frequencies. Around 9 m, the water depth increases again, the first harmonic amplitude continues decreasing and the third, fourth, and fifth harmonic amplitudes also begin to decrease, with an energy transfer to the second harmonic. Finally, in the shallowest part of the domain, the energy transfer from the second to the third harmonics begins again. The oscillations visible in the first and second harmonic amplitudes are likely caused by reflections from the lateral boundaries.

To further evaluate the spatial spectral evolution, a set of integral wave parameters are calculated. From the variance density spectrum ($E(f)$), the significant wave height $H_{m0} = 4\sqrt{m_0}$ and mean wave period $T_e = T_{m-1,0} = \frac{m_{-1}}{m_0}$ or $T_{m0,2} = (\frac{m_0}{m_2})^{\frac{1}{2}}$ can be expressed in terms of the n -th moment (m_n) of the variance density spectrum where $m_n = \int_0^\infty f^n E(f) df$. The 0^{th} moment corresponds to the free surface elevation variance or σ^2 (28).

Nonlinear effects are also visible in the spatial evolution of these parameters, which are globally estimated well by the model (Figure 15). The significant wave height evolves similarly to the first harmonic amplitude shown in Figure 14. It increases as the waves shoal, decreases in the trough and finally increases again as the water depth decreases approaching the beach.

The simulated H_{m0} agrees well with the measured values, with only a slight overestimation for $x > 7$ m and a maximum difference of 8.8%. The evolution of the mean wave period is similar for the two definitions considered ($T_{m-1,0}$ and $T_{m0,2}$). The mean period initially decreases when a reduction in the energy in the low frequency range of the spectrum is compensated by an increase in the high frequency range. The subsequent release of higher harmonics in the trough leads to an increase in the mean wave period that persists along the tank. The largest differences in mean period occur near the end of the tank, with errors of less than 3.5% and 7% for $T_{m-1,0}$ and $T_{m0,2}$, respectively.

To further analyze the simulated wave nonlinearity, the skewness (S) or horizontal asymmetry coefficient, vertical asymmetry coefficient (A) and kurtosis (K) are compared to those of the measurements. The skewness can be defined from the free surface elevation (26) or as:

$$S = \frac{\sum_{m=-\infty}^{+\infty} \sum_{n=-\infty}^{+\infty} \text{Re}[B_{m,n}]}{m_0^{3/2}}, \quad (29)$$

and the vertical asymmetry coefficient as:

$$A = \frac{\sum_{m=-\infty}^{+\infty} \sum_{n=-\infty}^{+\infty} \text{Im}[B_{m,n}]}{m_0^{3/2}}, \quad (30)$$

where $B_{m,n}$ is the complex bispectrum. Finally, the kurtosis measures the flattening of the free surface distribution, which is related to the probability of occurrence of high waves (27).

For a linear sea state, both the vertical and horizontal asymmetries are zero. Here (Figure 16), the simulated skewness and vertical asymmetry are approximately zero at the left side of the domain and evolve along the bathymetric profile in close agreement with the measurements. The spatial evolution of the kurtosis also begins with a value of approximately 3, typical of a linear (Gaussian) sea state, and then increases in shallower water, reaching a maximum in the shallowest zone. The model reproduces well the spatial evolution of the kurtosis, only slightly underestimating the maximum.

This test case validates the ability of the model to simulate the generation, propagation, and absorption of irregular, non-breaking waves, including nonlinear processes such as wave shoaling and wave interactions causing the transfer of energy between higher and lower harmonics.

4. Conclusions

Comparisons of simulation results to four laboratory experiments with non-breaking waves demonstrate that the model is able to simulate accurately nonlinear wave propagation, including nonlinear and dispersive effects. In the first set of experiments studying nonlinear resonant interactions in constant depth, the transfer of energy from the principal wave to its second harmonic was reproduced well, including the beat length of the resonant interaction. In the second case modeling the shoaling of highly nonlinear waves on a gentle beach, the model accurately simulated the changes in the wave profile, including the skewness and kurtosis, up to the breaking point. The last two sets of experiments investigated the propagation of regular and irregular nonlinear waves over a submerged bar and a barred beach, respectively, including the generation and propagation of higher-order harmonics. In both cases, the simulations reproduced well the observations, including the amplitudes of the first five harmonics.

Using the proposed spectral approach to solve for the velocity potential, the model converges exponentially with a flexible level of accuracy depending of the choice of N_T , the highest order Chebyshev polynomial. A sensitivity test verified previous results showing that the model simulates accurately wave propagation for $N_T = 7$ for real tests cases over variable bathymetry. To simulate well deep-water conditions, N_T can be increased to 10-12, as shown by the propagation of regular nonlinear waves over a flat bottom with relative water depths as high as $kh = 4\pi \approx 12.6$.

Ongoing model development includes taking into account the effects of wave breaking and validating the accuracy of simulations with moving bottoms (e.g. tsunami generation). The model is also currently being extended to 2DH using unstructured meshes to reach the objective of modeling the coastal zone.

5. Acknowledgments

Cécile Raoult's PhD thesis was funded partially by the French ANRT (Association Nationale de la Recherche et de la Technologie) with CIFRE grant 2013-1024.

6. References

- Agnon, Y., Madsen, P. A., Schäffer, H. A., 1999. A new approach to high-order Boussinesq models. *J. Fluid Mech.* 399, 319–333.
- Amestoy, P. R., Duff, I. S., Koster, J., L’Excellent, J.-Y., 2001. A fully synchronous multifrontal solver using distributed dynamic scheduling. *SIAM J. of Matrix Anal. and Appl.* 23 (1), 15–41.
- Amestoy, P. R., Guermouche, A., L’Excellent, J.-Y., Pralet, S., 2006. Hybrid scheduling for the parallel solution of linear systems. *Parallel Computing* 32, 136–156.
- Becq-Girard, F., Forget, P., Benoit, M., 1999. Non-linear propagation of unidirectional wave fields over varying topography. *Coast. Eng.* 38, 91–113.
- Beji, S., Battjes, J. A., 1993. Experimental investigation of wave propagation over a bar. *Coast. Eng.* 19, 151–162.
- Belibassakis, K. A., Athanassoulis, G. A., 2011. A coupled-mode system with application to nonlinear water waves propagating in finite water depth and in variable bathymetry regions. *Coast. Eng.* 58, 337–350.
- Bingham, H. B., Zhang, H., 2007. On the accuracy of finite-difference solutions for nonlinear water waves. *J. Eng. Math* 58, 211–228.
- Boyd, J. P., 2001. *Chebyshev and Fourier Spectral Methods: Second Edition, Revised*. Dover Publications, Mineola, NY, USA.
- Chapalain, G., Cointe, R., Temperville, A., 1992. Observed and modeled resonantly interacting progressive water-waves. *Coast. Eng.* 16, 267–300.
- Chazel, F., Benoit, M., Ern, A., Piperno, S., 2009. A double-layer Boussinesq-type model for highly nonlinear and dispersive waves. *Proc. R. Soc. A* 465, 2319–2346.
- Chern, M. J., Borthwick, A. G. L., Eatock Taylor, R., 1999. A pseudospectral σ -transformation model of 2-D nonlinear waves. *J. Fluids Structures* 13, 607–630.

- Christiansen, T. B., Engsig-Karup, A. P., Bingham, H. B., 2013. Hybrid-spectral model for fully nonlinear numerical wave tank. In: Proceedings of the 28th International Workshop on Water Waves and Floating Bodies. L’Isle-sur-la-Sorgue, France, 4p.
- Clamond, D., Grue, J., 2001. A fast method for fully nonlinear water-wave computations. *J. Fluid Mech.* 447, 337–355.
- Dalrymple, R. A., Herault, A., Bilotta, G., Farahani, R., 2011. GPU-Accelerated SPH model for water waves and free surface flows. *Coastal Engineering Proceedings* 1 (32), 9 p.
- Dalrymple, R. A., Rogers, B. D., 2006. Numerical modeling of water waves with the SPH method. *Coast. Eng.* 53, 141–147.
- Dingemans, M., 1994. Comparison of computations with Boussinesq-like models and laboratory measurements. Mast-G8M technical report, Delft Hydraulics, Delft, The Netherlands.
- Dombre, E., Benoit, M., Violeau, D., Peyrard, C., 2015. Simulation of floating structure dynamics in waves by implicit coupling of a fully non-linear potential flow model and rigid body motion approach. *J. Ocean Eng. Mar. Energy* 1, 55–76.
- Dommermuth, D. G., Yue, D. K. P., 1987. A high-order spectral method for the study of nonlinear gravity waves. *J. Fluid Mech.* 184, 267–288.
- Ducrozet, G., Bingham, H. B., Engsig-Karup, A. P., Bonnefoy, F., Ferrant, P., 2012. A comparative study of two fast nonlinear free-surface water wave models. *Int. J. Numer. Meth. Fluids* 69 (11), 18181834.
- Engsig-Karup, A. P., Bingham, H. B., Lindberg, O., 2009. An efficient flexible-order model for 3D nonlinear water waves. *J. Comp. Phys.* 228, 2100–2118.
- Engsig-Karup, A. P., Hesthaven, J. S., Bingham, H. B., Madsen, P. A., 2006. Nodal DG-FEM solution of high-order Boussinesq-type equations. *J. Eng. Math* 56 (3), 351–370.
- Fochesato, C., Grilli, S. T., Dias, F., 2007. Numerical modeling of extreme rogue waves generated by directional energy focusing. *Wave Motion* 44, 395–416.

- Fornberg, B., 1988. Generation of finite difference formulas on arbitrarily spaced grids. *Mathematics of Computation* 51 (184), 699–706.
- Fructus, D., Clamond, D., Grue, J., Kristiansen, Ø., 2005. An efficient model for three-dimensional surface wave simulations: Part I: Free space problems. *J. Comp. Phys.* 205, 665–685.
- Fructus, D., Grue, J., 2007. An explicit method for the nonlinear interaction between water waves and variable and moving bottom topography. *J. Comp. Phys.* 222, 720–739.
- Fuhrman, D. R., Bingham, H. B., 2004. Numerical solution of fully non-linear and highly dispersive Boussinesq equations in two horizontal dimensions. *Int. J. Numer. Meth. Fluids* 44, 231–255.
- Gouin, M., Ducrozet, G., Ferrant, P., 2015. Validation of a nonlinear spectral model for water waves over a variable bathymetry. In: *30th International Workshop on Water Waves and Floating Bodies*. Bristol, UK, 4 p.
- Grilli, S. T., Skourup, J., Svendsen, I. A., 1989. An efficient boundary element method for nonlinear water waves. *Eng. Anal. Bound. Elem.* 6 (2), 97–107.
- Guyenne, P., Nicholls, D. P., 2007. A high-order spectral method for nonlinear water waves over moving bottom topography. *SIAM J. Sci. Comput.* 30 (1), 81–101.
- Higuera, P., Lara, J. L., Losada, I. J., 2013a. Realistic wave generation and active wave absorption for Navier-Stokes Application to OpenFOAM®. *Coast. Eng.* 71, 102–118.
- Higuera, P., Lara, J. L., Losada, I. J., 2013b. Simulating coastal engineering processes with OpenFOAM®. *Coast. Eng.* 71, 119–134.
- Kennedy, A. B., Fenton, J. D., 1997. A fully-nonlinear computational method for wave propagation over topography. *Coast. Eng.* 32, 137–161.
- Kennedy, A. B., Kirby, J. T., Chen, Q., Dalrymple, R. A., 2001. Boussinesq-type equations with improved nonlinear performance. *Wave Motion* 33, 225–243.

- 1
- 2
- 3
- 4
- 5
- 6
- 7
- 8
- 9 Kirby, J. T., 2003. Boussinesq models and applications to nearshore
10 wave propagation, surfzone processes and wave-induced currents. In:
11 V. C. Lakhan, E. (Ed.), *Advances in Coastal Modeling*. pp. 1–31.
- 12
- 13 Kreiss, H.-O., Oliger, J., 1972. Comparison of accurate methods for the in-
14 tegration of hyperbolic equations. *Telus* XXIV 3, 199–215.
- 15
- 16
- 17 Lara, J. L., Garcia, N., Losada, I. J., 2006. RANS modelling applied to ran-
18 dom wave interaction with submerged permeable structures. *Coast. Eng.*
19 53, 395–417.
- 20
- 21
- 22 Li, B., Fleming, C., 1997. A three dimensional multigrid model for fully
23 nonlinear water waves. *Coast. Eng.* 30, 235–258.
- 24
- 25 Lynett, P., Liu, P. L.-F., 2004. A two-layer approach to wave modelling.
26 *Proc. R. Soc. A* 460, 2637–2669.
- 27
- 28 Ma, Q. W., Wu, G. X., Taylor, R. E., 2001. Finite element simulation of fully
29 non-linear interaction between vertical cylinders and steep waves. Part 1:
30 Methodology and numerical procedure. *Int. J. Numer. Meth. Fluids* 36,
31 265–285.
- 32
- 33
- 34 Madsen, P. A., Bingham, H. B., Liu, H., 2002. A new Boussinesq method
35 for fully nonlinear waves from shallow to deep water. *J. Fluid Mech.* 462,
36 1–30.
- 37
- 38
- 39 Madsen, P. A., Schäffer, H. A., 1998. Higher order Boussinesq-type equations
40 for surface gravity waves: derivation and analysis. *Phil. Trans. R. Soc. A*
41 356, 31233181.
- 42
- 43 Narayanaswamy, M., Cabrera Crespo, A. J., Gómez-Gesteira, M., 2010.
44 SPHysics-FUNWAVE hybrid model for coastal wave propagation. *J. Hy-*
45 *draul. Res.* 48, 85–93.
- 46
- 47
- 48 Newman, J. N., Lee, C.-H., 2002. Boundary-Element Methods in offshore
49 structure analysis. *J. Offshore Mech. Arctic Eng.* 124, 81–89.
- 50
- 51
- 52 Shao, S., 2006. Incompressible SPH simulation of wave breaking and overtop-
53 ping with turbulence modelling. *Int. J. Numer. Meth. Fluids* 50, 597–621.
- 54
- 55 Smith, R. A., 1998. An operator expansion formalism for nonlinear surface
56 waves over variable depth. *J. Fluid Mech.* 363, 333–347.
- 57
- 58
- 59
- 60
- 61
- 62
- 63
- 64
- 65

- Stelling, G., Zijlema, M., 2003. An accurate and efficient finite-difference algorithm for non-hydrostatic free-surface flow with application to wave propagation. *Int. J. Numer. Meth. Fluids* 43, 1–23.
- Tian, Y., Sato, S., 2008. A numerical model on the interaction between nearshore nonlinear waves and strong currents. *Coast. Eng. Journal* 50 (4), 369–395.
- Ting, F. C. K., Kirby, J. T., 1994. Observation of undertow and turbulence in a laboratory surf zone. *Coast. Eng.* 24, 51–80.
- Wang, P., Yao, Y., Tulin, M., 1995. An efficient numerical tank for nonlinear water waves, based on the multi-subdomain approach with BEM. *Int. J. Numer. Meth. Fluids* 20, 1315–1336.
- West, B. J., Brueckner, K. A., Janda, R. S., Milder, M., Milton, R. L., 1987. A new numerical method for surface hydrodynamics. *J. Geophys. Res.* 92, 11803–11824.
- Wu, G. X., Ma, Q. W., Taylor, R. E., 1998. Numerical simulation of sloshing waves in a 3D tank based on a finite element method. *Appl. Ocean Res.* 20, 337–355.
- Yates, M. L., Benoit, M., 2015. Accuracy and efficiency of two numerical methods of solving the potential flow problem for highly nonlinear and dispersive water waves. *Int. J. Numer. Meth. Fluids* 77, 616–640.
- Zakharov, V. E., 1968. Stability of periodic waves of finite amplitude on the surface of a deep fluid. *J. Appl. Mech. Tech. Phys.* 9 (2), 190–194.
- Zhao, B. B., Ertekin, R. C., Duan, W. Y., Hayatdavoodi, M., 2014. On the steady solitary-wave solution of the Green-Naghdi equations of different levels. *Wave Motion* 51, 1382–1395.
- Zhu, L., Chen, Q., Wan, X., 2014. Optimization of non-hydrostatic Euler model for water waves. *Coast. Eng.* 91, 191–199.
- Zijlema, M., Stelling, G. S., 2005. Further experiences with computing non-hydrostatic free-surface flows involving water waves. *Int. J. Numer. Meth. Fluids* 48, 169–197.

Ziljema, M., Stelling, G. S., 2008. Efficient computation of surf zone waves using the nonlinear shallow water equations with non-hydrostatic pressure. Coast. Eng. 55, 780–790.

Ziljema, M., Stelling, G. S., Smit, P., 2011. SWASH: An operational public domain code for simulating wave fields and rapidly varied flows in coastal waters. Coast. Eng. 58, 992–1012.

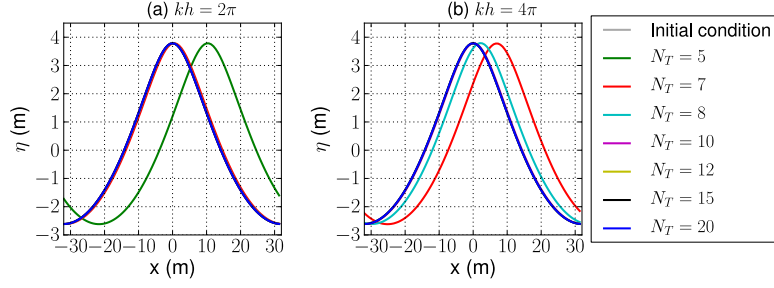


Figure 1: Simulated free surface position for a range of N_T (highest order Chebyshev polynomial) after 25 periods of wave propagation for (a) $kh = 2\pi$ and (b) $kh = 4\pi$.

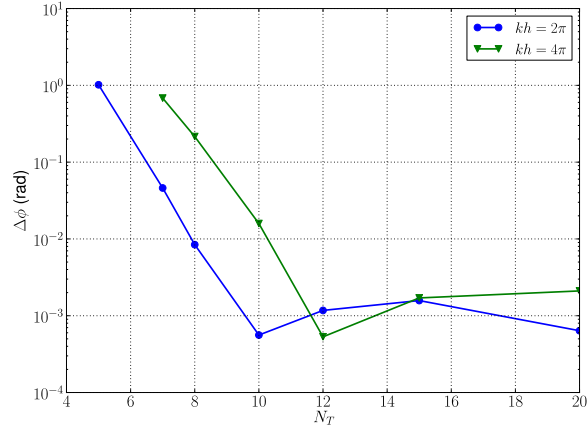


Figure 2: Phase difference as a function of N_T (highest order Chebyshev polynomial) after 25 periods of wave propagation for the simulations shown in Figure 1.

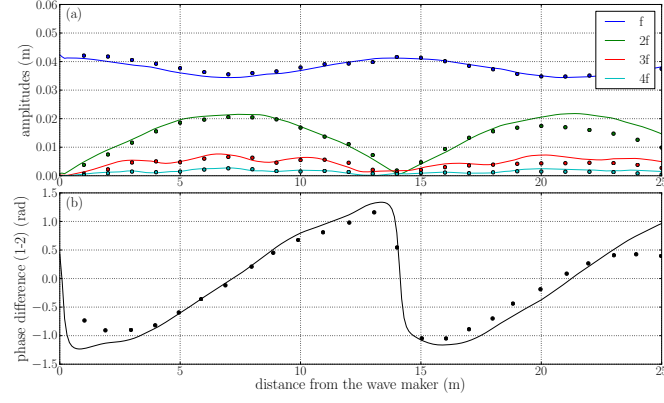


Figure 3: a) Spatial evolution of the first four harmonic amplitudes for test case A of Chapalain et al. (1992): experimental (circles) and MISTHYC simulation (solid line) results. b) Spatial evolution of the phase difference between the first and second harmonic: experimental (C92, circles) and MISTHYC simulation (solid line) results.

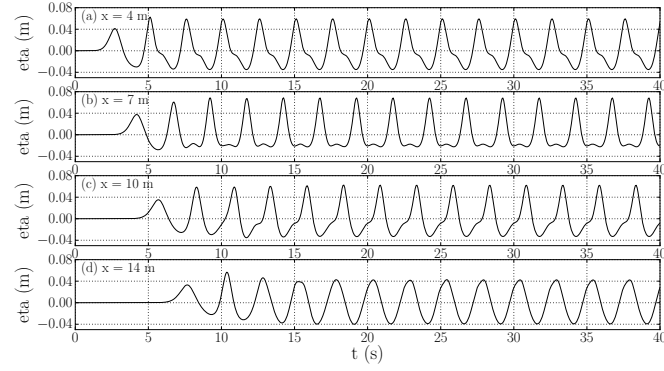


Figure 4: MISTHYC simulated free surface elevation η at four different positions in the wave channel for the test case A of Chapalain et al. (1992).

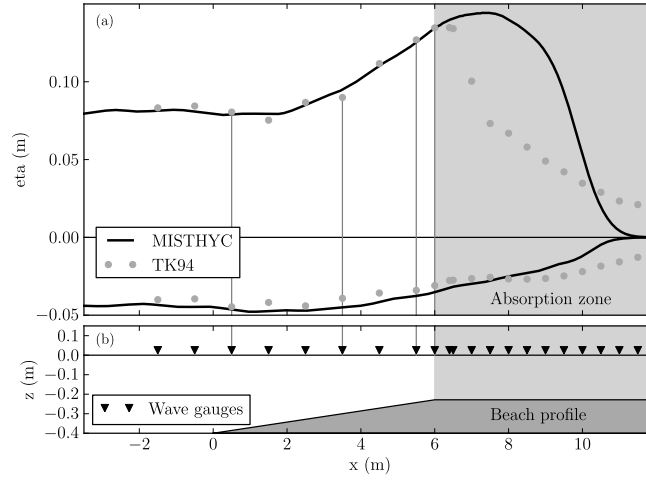


Figure 5: (a) Minimum and maximum free surface elevation η from the MISTHYC simulations in comparison to the wave gauge measurements of Ting and Kirby (1994) for a regular nonlinear wave with $H = 0.125$ m and $T = 2.0$ s. (b) Beach profile used in the model simulations, showing the location of the wave gauges. In (a) and (b), the light gray shaded area ($x \geq 6$ m) indicates the wave absorption zone, and the vertical gray lines indicate the wave gauge measurements shown in Figure 6.

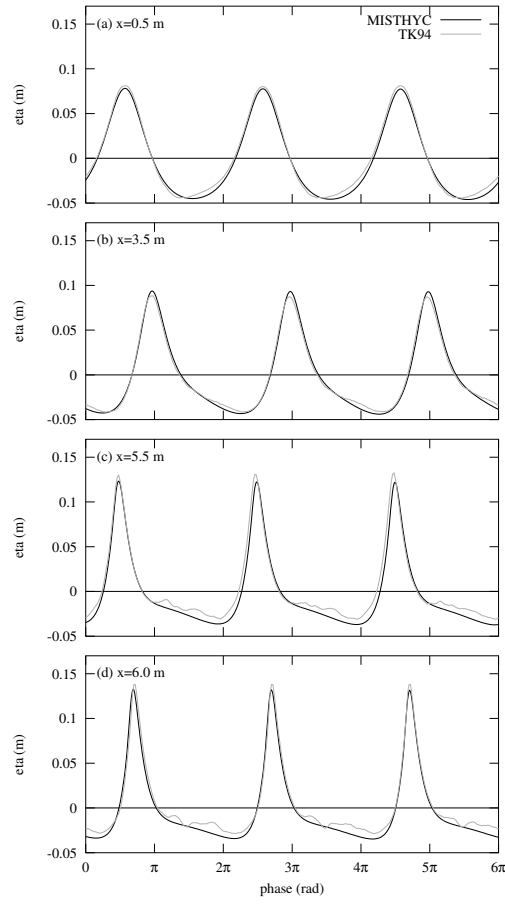


Figure 6: Simulated and measured (Ting and Kirby, 1994) free surface elevation time series at waves gauges located at: (a) $x = 0.5$ m, (b) $x = 3.5$ m, (c) $x = 5.5$ m, and (d) $x = 6.0$ m (indicated by the vertical gray lines in Figure 5).

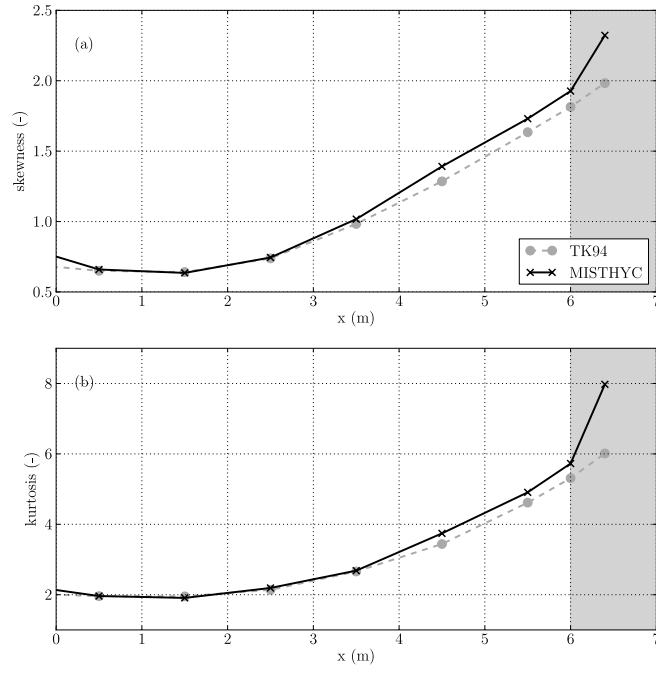


Figure 7: Simulated and measured (Ting and Kirby, 1994) wave skewness and kurtosis at wave gauges leading up to and in the beginning of the wave absorption zone (light gray shaded area starting at $x = 6.0$ m).

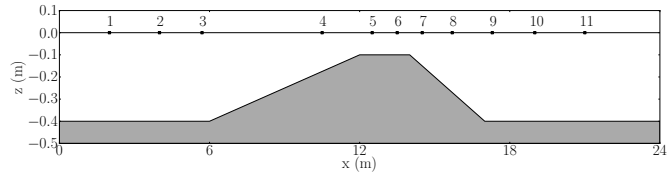


Figure 8: Bathymetry and position of wave probes in the Dingemans (1994) experiments.

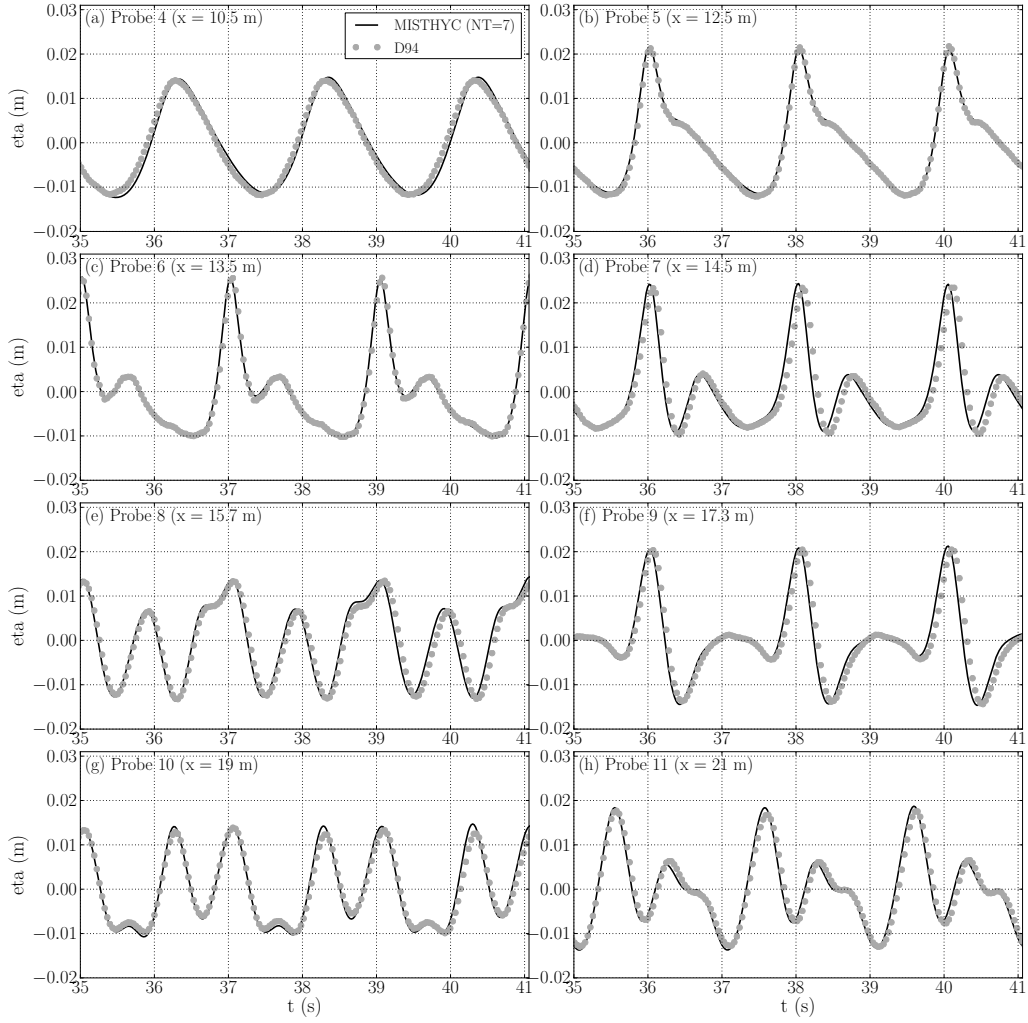


Figure 9: Comparison of measured and simulated (with $N_T = 7$) free surface elevation time series at probes 4 to 11 for case A of Dingemans (1994) (probe location in Figure 8).

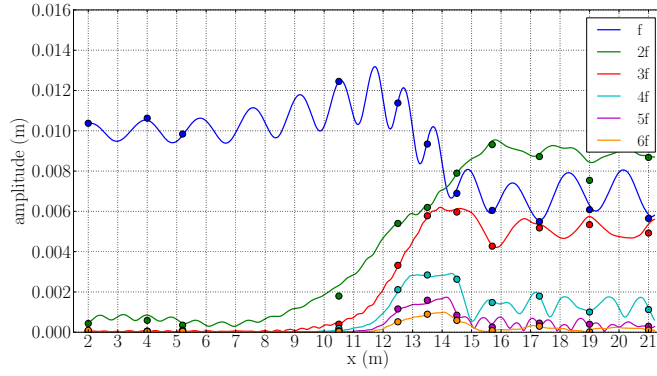


Figure 10: Spatial evolution of the first six harmonic amplitudes (at frequencies f , $2f$, ..., $6f$) of the free surface elevation for case A of Dingemans (1994) experiments: observations (D94, circles) and MISTHYC simulation results (solid lines) .

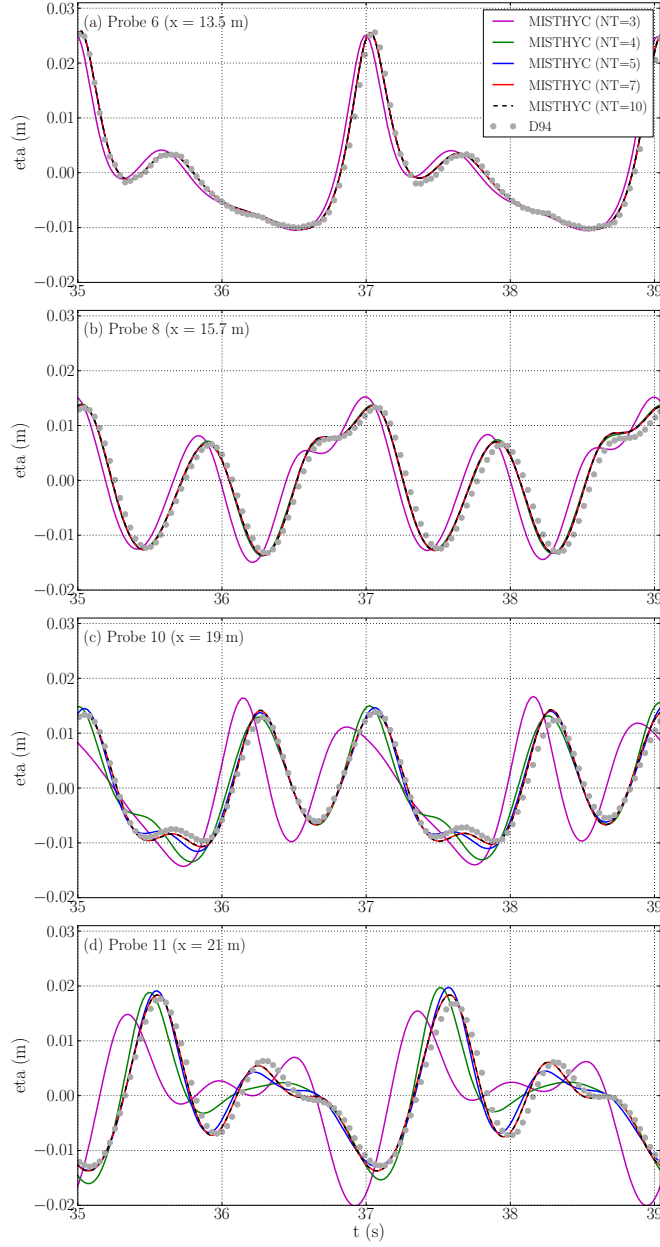


Figure 11: Comparison of measured and simulated free surface elevation time series at probes 6, 8, 10 and 11 for case A of Dingemans (1994). Results of simulations with 5 values of N_T (3, 4, 5, 7, 10) are compared (all other numerical parameters are constant).